Stacking effects on the electronic and optical properties of bilayer transition metal dichalcogenides MoS_2, $MoSe_2$, WS_2, and WSe_2

Jiangang He,[1,2] Kerstin Hummer,[1] and Cesare Franchini[1,*]

[1]*University of Vienna, Faculty of Physics, Department of Computational Materials Physics, Sensengasse 8/12, 1090 Vienna, Austria*

[2]*School of Applied & Engineering Physics, Cornell University, Ithaca, New York, USA*

(Received 26 November 2013; revised manuscript received 26 January 2014; published 10 February 2014)

Employing the random phase approximation we investigate the binding energy and Van der Waals (vdW) interlayer spacing between the two layers of bilayer transition metal dichalcogenides MoS_2, $MoSe_2$, WS_2, and WSe_2 for five different stacking patterns, and examine the stacking-induced modifications on the electronic and optical/excitonic properties within the GW approximation with *a priori* inclusion of spin-orbit coupling and by solving the two-particle Bethe-Salpeter equation. Our results show that for all cases, the most stable stacking order is the high symmetry AA' type, distinctive of the bulklike $2H$ symmetry, followed by the AB stacking fault, typical of the $3R$ polytypism, which is by only 5 meV/formula unit less stable. The conduction band minimum is always located in the midpoint between K and Γ, regardless of the stacking and chemical composition. All MX_2 undergo an direct-to-indirect optical gap transition going from the monolayer to the bilayer regime. The stacking and the characteristic vdW interlayer distance mainly influence the valence band splitting at K and its relative energy with respect to Γ, as well as, the electron-hole binding energy and the values of the optical excitations.

DOI: 10.1103/PhysRevB.89.075409 PACS number(s): 71.15.Nc, 61.30.Hn, 73.22.−f, 78.67.−n

I. INTRODUCTION

The pioneering achievements in the fabrication of atomically thin layered materials by mechanical exfoliation as demonstrated by Novoselov *et al.* [1,2] have enabled explorations of novel physical properties exclusively inherent to low-dimensional structures. As exemplified by surface states of massless Dirac fermions [3] and the anomalous quantum Hall effect observed in graphene [4], the physics of two-dimensional (2D) electron systems have attracted massively growing attention. Apart from graphene [5,6], layered materials also exhibit extraordinary physics that can be achieved by low-dimensional structuring [7]. Prominent examples in this respect are the VA-VIA systems (Bi_2Te_3 and Bi_2Se_3) that show topologically protected metallic surface states up to room temperature [8], hexagonal boron nitride (h-BN), oxides such as titania, and transition metal dichalcogenides (MX_2) [9].

The layered MX_2 with M = Mo, W, and X = S, Se consist of stacked X-M-X layers, where the hexagonally packed metal atoms M are typically trigonal prismatic coordinated with the X atom. The M-X bonds within one layer are covalent (strong intralayer interactions), whereas the interlayer interaction are of the van der Waals (vdW) type. The inherent weakness of the vdW forces can induce stacking faults (i.e., mutual sliding of adjacent layers), which result in different stacking sequences and therefore in different polytypisms [10–12]. Sliding systems subjected to stacking faults such as MX_2 and h-BN are widely exploited as solid lubricant additives [13,14] and have become the subject of high-level theoretical studies aiming to determine the most favorable stacking orders [12,15].

Among MX_2 materials, the prototype molybdenum disulfide (MoS_2) has attracted intense interest because of its distinct mechanical, electronic, optical, and catalytic properties important for application in dry lubrication [16], photovoltaics [17], and photocatalysis [18]. In particular since 2005, when monolayer (ML) MoS_2 was obtained using microexfoliation techniques [2], atomically thin layers of MX_2 are actively investigated.

While bulk $MoS_2$is an indirect gap semiconductor with a band gap of ∼1.3 eV [19,20], ML MoS_2 is a direct-gap semiconductor with a band gap of 1.8–1.9 eV [21,22]. Such a transition from an indirect to a direct-gap semiconductor was also observed in $WS_2$and WSe_2 [23–25] making such MX_2 monolayers in nanoelectronics applications superior to pristine graphene that has no band gap. Intriguingly, the presence of several conduction and valence band valleys could open up the way towards the realization of valleytronics devices, based on the possibility of selectively confining the charge carriers in a restricted portion of the momentum space [26,27]. For example, Radisavljevic *et al.* demonstrated that suitable carrier mobilities are achieved in a MoS_2 monolayer field effect transistor by covering the MoS_2 monolayer with hafnium oxide [28]. Alternatively, bipolar field effect transistors based on graphene heterostructures with atomically thin MoS_2or h-BN also revealed promising characteristics regarding carrier mobilities and current on/off ratios [29].

Recent experimental and theoretical investigations of MoS_2 demonstrate that the phonon dispersion relations [21,30,31] as well as the band gap and exciton binding energies [32] show interesting quantum confinement effects, when the layer thickness is reduced. In the monolayer limit, the optical absorption and photoluminescence quantum yield of ML $MoS_2$is tremendously enhanced and two strongly bound exciton peaks (A and B) located at 1.8 and 1.9 eV were observed [21,22]. The origin of this double-peak structure in the optical absorption spectra has been discussed in several theoretical studies [33–36]. Finally, elaborate calculations using the GW [37,38] approach explicitly including spin-orbit coupling (SOC) and subsequently solving the Bethe-Salpeter equation (BSE) [39] to account for the electron-hole interaction could confirm that these A and B excitons arise from the split valence band maximum due to SOC [40]. Also the strain effects on the direct band gap of ML MoS_2 have been investigated by means of

*cesare.franchini@univie.ac.at

density functional theory (DFT) combined with self-consistent GW and BSE [35]. These studies revealed that ML MoS_2 transforms to an indirect gap semiconductor under ∼1.5% tensile strain.

Bilayer (BL) MX_2 is the first MX_2 multilayer system involving vdW interactions. In contrast to ML MoS_2, BL $MoS_2$is an indirect gap semiconductor exhibiting rather bulk-like electronic properties [41–45]. The transition from direct gap ML to indirect gap BL was attributed to these interlayer interactions and to the particularly pronounced thickness dependence of the Mo $4d$ states comprising the valence and conduction bands [43]. However, the equilibrium distance between two layers, the strength of van der Waals forces or binding energies between two layers, the most favorable stacking pattern, and the relationship between electronic structures and stacking and van der Waals interactions are still unclear.

The aim of the present study is to determine the most favorable stacking order in bilayer MX_2 and to examine the stacking-induced modifications on the electronic band structure and absorption spectra within a many-body framework including the random phase approximation (RPA) for the structural and energetic properties, and the GW approximation combined with the Bethe-Salpeter equation (BSE) for the electronic and optical properties, respectively.

II. CRYSTAL STRUCTURE AND VAN DER WAALS INTERACTIONS

Natural or synthetic MX_2 crystallize in two different polytypisms, $2H$ (space group: $P6_3/mmc$) and $3R$ (space group: $R3m$), with the former being the dominating one. In both phases the M atom in one layer is aligned over the X atom in the layer beneath, but the lateral registry is different: in $2H$ the X atoms are fully eclipsed (eclipsed AA' stacking, according to the nomenclature proposed in Ref. [12]), whereas in the $3R$ geometry the X atoms are staggered, i.e., one X is eclipsed by the M atom above and the second one is located below the hexagonal hollow site, resulting in the staggered AB stacking (see Fig. 1).

In this study we consider all five possible high-symmetry stacking orders, which are depicted in Fig. 1: (i) AA (point group D_{3h}), eclipsed stacking with M over M and X over X; (ii) AA' (point group D_{3d}), eclipsed stacking with M over X, characteristic of the $2H$ phase; (iii) $A'B$ (point group D_{3d}), staggered stacking with X over X; (iv) AB (point group C_{3v}), staggered stacking with X over M, characteristic of the $3R$ phase; (v) AB' (point group D_{3d}), staggered stacking with M over M. It is readily seen that one can transform one stacking polytypism into another by horizontal layer sliding and/or by rotation around the vertical axis.

A parameter-free theoretical description of dispersion forces is still a challenge and requires computational techniques beyond the standard (semi)local exchange-correlation functionals commonly adopted in DFT calculations such as the local density approximation (LDA) [46] or the generalized gradient approximation (GGA) [47]. These are not capable to correctly account for vdW interactions. Popular remedies to cure the lack of vdW interactions consist of adding a semiempirical pairwise interatomic dispersion interaction

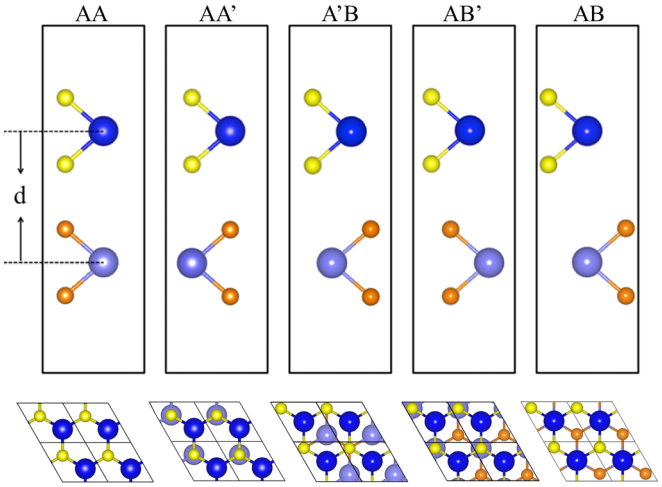

FIG. 1. (Color online) Side (upper panel) and top (lower panel) views of the high-symmetry stacking orders of bilayer MX_2. We follow the nomenclature proposed in Ref. [12]. Large and small spheres represent the M and X atomic species, respectively. A grayscale (color coding) is used to distinguish the position of the atoms in the two MX_2 layers. The full lines demarcate the unit cell.

on top of standard DFT. These approaches are commonly referred to as DFT-D methods, where the accuracy of the results crucially depends on the approximations involved in computing the dispersion coefficients and on the cutoff function that damps off the vdW contributions at short distances [48–52]. Improvements can be also achieved by including nonlocal (i.e., long-range) correlations to (semi)local correlation functionals. The resulting methods known as van der Waals density functionals (vdW-DF) do not rely on predetermined input parameters for the calculation of the dispersion coefficients, which are now evaluated directly from the electron density [50,53,54].

An alternative way to describe the vdW interaction is based on methods that go beyond the pairwise approximation by directly calculating the correlation energy. The most representative ones are the adiabatic-connection fluctuation-dissipation theorem (ACFDT) [55] within the the random phase approximation (RPA) [56–58], and post-Hartee-Fock methods such as coupled cluster and the second-order Møller-Plesset perturbation theory [59]. Though computationally very expensive, these methods provide the most accurate description of dispersion forces and have been successfully applied to layered materials including graphite, h-BN bilayers, as well as graphene absorption on metal surfaces [12,60–63].

In our study, the nonlocal dispersion forces are described by ACFDT-RPA (hereafter termed RPA). Based on the optimized RPA structures, the effect of confinement (monolayer-bilayer/bulk) as well as the layer stacking on the electronic and optical properties are calculated using the GW approximation in combination with BSE including the effects of SOC.

III. COMPUTATIONAL DETAILS

In this paper, all calculations were performed by using the Vienna *ab initio* Simulation Package (VASP) [67,68], where the electron and ion interaction is described within the projector

TABLE I. Experimental structure parameters of bulk MX_2 (M = Mo and W; X = S and Se). a, c, b_{MX}, b_{XX}, and δ denote hexagonal lattice constants, the M-X and X-X bond lengths, and the X-M-X bond angle, respectively.

	MoS_2[a]	$MoSe_2$[b]	WS_2[c]	WSe_2[d]
a (Å)	3.160	3.288	3.153	3.282
c (Å)	12.29	12.90	12.32	12.96
b_{MX} (Å)	2.42	2.52	2.40	2.53
b_{XX} (Å)	3.17	3.33	3.14	3.34
δ (°)	82.00	82.48	81.60	82.80

[a]Reference [64].
[b]Reference [65].
[c]Reference [66].
[d]Reference [66].

augmented wave method [69,70]. Based on the bulk MX_2 structures, whose structural details are summarized in Table I, we adopted a slab setup consisting of two MX_2layers. Five different stacking sequences (see Fig. 1) were considered. A vacuum region of 20 Å along the c direction was used to separate the bilayer systems in order to avoid spurious interactions due to the nonlocal nature of the correlation energy [63]. The vdW interlayer distance was optimized on the basis of the RPA theory by computing the total energy as a function of the interlayer distance d, for about 25 values of d ranging between 5 Å and 13 Å. Since the calculation of forces is not yet possible on the level of RPA, all calculations in the present work are based on the experimentally determined bulk structural parameters of MX_2 (in-plane lattice constant a and internal atomic positions b_{MX}, b_{XX}, and δ) as given in Table I.

For each bilayer structure with a given d, the total energy (E_{TOT}) was calculated by summing the exact exchange energy (E_{EXX}) with the corresponding RPA correlation energy (E_{C}). In the EXX calculations a plane-wave cutoff of 600 eV and a $16 \times 16 \times 2$ Γ-centered **k**-point mesh was used. To calculate the correlation energy at RPA level, the plane wave cutoff and the **k**-point mesh were reduced to 500 eV and $6 \times 6 \times 1$, respectively. These parameters yielded very well converged EXX and RPA correlation energies.

For comparison, DFT calculations including dispersion correction within the DFT-D2 (PBE-D2 [48]) and vdW-DF (optB88-vdW [54]) prescriptions, as well as DFT without dispersion corrections were also performed. In the latter case the PBEsol exchange-correlation functional [71] was considered, which was designed to improve GGA performance on solids and surfaces and was found to work well on van der Waals systems too [12,72]. A $16 \times 16 \times 1$ Γ-centered k-mesh and a plane wave energy cutoff of 600 and 500 eV were used for DFT-D2 and vdW-DF/PBEsol, respectively. In order to be fully consistent with the RPA structural setup, also for the DFT-based calculations we used the bulk in-plane lattice constant and atomic positions. However, we should underline that the vdW-DF optimized structural data are in almost unchanged with respect to the experimental ones and are not much affected by the stacking order, as shown in Table II for BL MoS_2.

TABLE II. Comparison between the vdW-DF fully relaxed structural parameters of BL MoS_2 (the in-plane lattice constant a, the Mo-S bond length, the S-S bond length, and the S-Mo-S bond angle δ) and the corresponding bulk experimental values [64].

Stacking	a (Å)	Mo-S (Å)	S-S (Å)	δ (°)
AA	3.164	2.407	3.135	81.3
AA'	3.166	2.407	3.143	81.5
$A'B$	3.164	2.407	3.135	81.3
AB	3.166	2.408	3.135	81.2
AB'	3.168	2.410	3.136	81.2
Bulk (Expt.)	3.160	2.417	3.172	82.0

The electronic structures were studied by using the G_0W_0+SOC approximation, with 400 eV plane-wave cutoff, a total of 256 occupied and virtual states, and a $18 \times 18 \times 1$ Γ-centered **k**-point mesh. We used the WANNIER90 code [73] and the VASP2WANNIER90 interface [74] to interpolate the band structures to a finer grid. Finally, the optical absorption spectra were obtained on the level of BSE@G_0W_0, by using a $18 \times 18 \times 1$ Γ-centered **k**-mesh.

IV. RESULTS

A. Energetics of the geometrical structures

Starting from the experimental structure data given in Table I the equilibrium distance d_0 between two MX_2 layers was determined by varying the interlayer distance d as defined in Fig. 1 from 5 Å to 13 Å while keeping the in-plane lattice constant a fixed at the MX_2 bulk value. This procedure is justified, since the in-plane lattice constant is dominated by covalent interactions and thus not sensitive to the interlayer distance. The resulting RPA total energy curves for MoS_2, $MoSe_2$, WS_2, and WSe_2 in the five considered stacking orders are collected in Fig. 2.

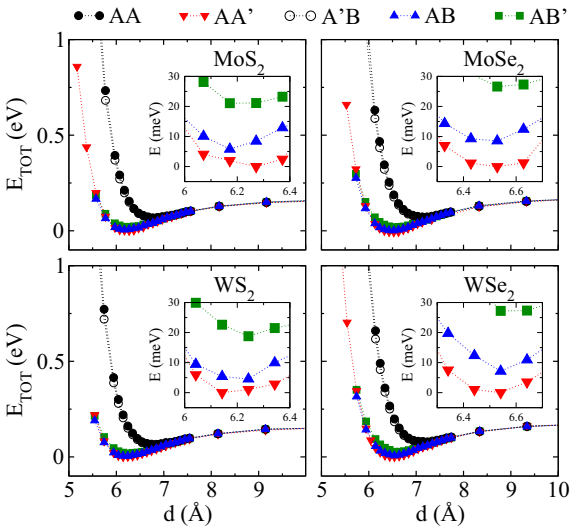

FIG. 2. (Color online) The EXX+RPA total energy E_{TOT} as a function of the interlayer distance d for the five differently stacked MX_2 bilayers (see Fig. 1). Insets: zoom near the minimum. Energies are given with respect to the most stable AA' total energy.

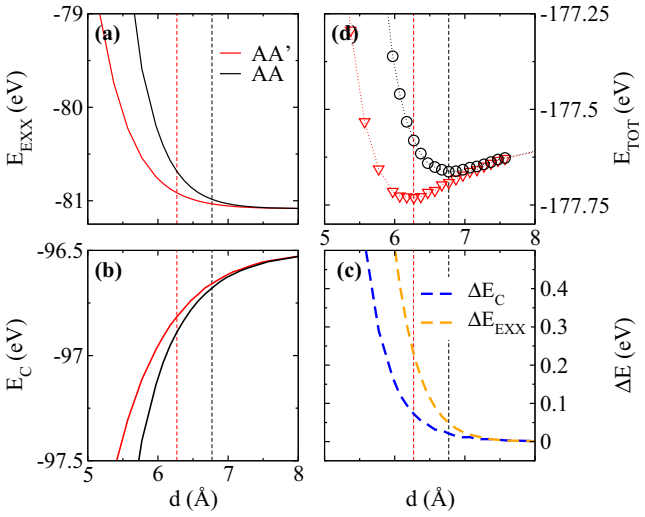

FIG. 3. (Color online) Evolution of $E_{\rm EXX}$ (a) and $E_{\rm C}$ (b) in AA' and AA ordered MoS_2 bilayers as a function of d. (c) Difference of the correlation and EXX energies between the AA' and AA ordered MoS_2 bilayer. (d) Total energy given as a sum of $E_{\rm EXX} + E_{\rm C}$. The vertical dashed lines indicate d_0 in AA' (6.27 Å) and in AA (6.77 Å).

It is evident from the total energy curves of Fig. 2 that all four MX_2 compounds exhibit a very similar behavior. The most stable stacking pattern is AA', which is by only $\approx$5 meV per formula unit (f.u.) more stable than the AB sequence. This small energy difference explains the occurrence of these two stacking orders in the natural bulk forms $2H$ (AA') and $3R$ (AB) and confirms the level of accuracy of RPA-type approaches. The next most stable stacking order is AB', about 20 meV/f.u. less stable than AA'. The remaining high symmetry stacking AA and $A'B$ are significantly less bounded, by almost 40 meV/f.u. The overall relative stability trend ($AA' \simeq AB > AB' \gg AA \simeq A'B$) is similar to the one predicted for h-BN [11,12,75]. Adopting the colloquial terminology of Liu *et al.* we name the two different groups of stackings "good" (AA', AB, and AB') and "bad" (AA and $A'B$) according to their stabilities [11].

In the case of h-BN, the weaker stability of the AA and $A'B$ stackings was attributed to electrostatic interactions [75]. In MX_2 compounds, important conclusions on the competition between vdW and electrostatic interactions can be achieved by directly comparing the evolution of E_{EXX} and E_C as a function of d in good and bad stackings [12]. The results for AA' and AA stacked MoS_2 are shown in Fig. 3. As expected, E_{EXX} and E_C follow an opposite trend with increasing interlayer distance d as shown in Figs. 3(a) and 3(b), respectively. The delicate balance between these two contributions leads to a minimum at a certain interlayer distance d_0, which is significantly larger in AA (6.77 Å) compared to AA' (6.27 Å), as reported in Table III. The reason behind the weak stability of the AA is readily elucidated by considering the difference of the correlation and EXX energies in the AA' and AA, i.e., $\Delta E_C = E_C^{AA'} - E_C^{AA}$ and $\Delta E_{EXX} = E_{EXX}^{AA} - E_{EXX}^{AA'}$. The results illustrated in Fig. 3(c) convey the following messages: (i) ΔE_{EXX} is considerably larger than ΔE_C, indicating that the energy difference between the two stackings comes from Pauli repulsion. More quantitatively, close to the minimum (in the region near the optimized interlayer distances, indicated by the vertical dashed lines in Fig. 3) the AA and AA' have very similar correlation energy (the energy difference is less than 50 mev), whereas the EXX energy is up to 200 meV larger in the AA registry. Thus, the lower stability of the AA stacking should be attributed to a more repulsive force between the two layers: this is usually related to stronger Pauli repulsions, caused by a more pronounced overlap of electron densities (steric effect). (ii) The difference between ΔE_{EXX} and ΔE_C is progressively attenuated with increasing d, which explains why the AA stacking is stabilized at larger interlayer distance. The same conclusions apply to the other good and bad stackings in the various MX_2 compounds. Namely, for all bad stackings $\Delta E_{EXX} > \Delta E_C$ and the interlayer distances are always larger by more than 0.5 Å than the ones of the good structures.

In order to benchmark the DFT based results (DFT-D2, vdW-DF, and PBEsol) with those obtained by RPA, a complete set of equilibrium interlayer distances d_0, ground-state energies E_0, and binding energies E_b are listed in Table III together with available experimental data for the corresponding bulk systems. The E_b is evaluated as energy difference between the total energy values at d_0 and $d = 13$Å, which well approximates the limit of infinite layer distance.

For clearly visualizing the subtle differences and trends, a graphical analysis of the full set of data summarized in Table III is provided in Fig. 4. Therein, the optimized interlayer distances d_0 and the binding energies E_b with respect to the corresponding RPA findings are depicted.

For d_0 [see Fig. 4(a)], DFT-D2 and vdW-DF perform exceedingly well in computing d_0, especially for the most stable AA' stacking, with relative deviations smaller than 1%. PBEsol yields satisfactory results for the AA' and AB phases (within 1–2%), but severely overestimates d_0 for the other stackings with errors as high as 8%.

In the following, binding energies (E_b) and relative stabilities (ΔE_0) are considered. Distinguished in Table III, PBEsol severely underestimates the ΔE_0 as well as the binding energies E_b. While vdW-DF yields almost identical results to the RPA for ΔE_0, it overestimates the binding energies by roughly 30 meV/f.u. in all cases. In contrast to vdW-DF, the trends are materials specific when comparing the DFT-D2 results to the RPA. In the case of MoS_2 structures, the DFT-D2 functional slightly underestimates ΔE_0, whereas the ΔE_0 of the WS_2 stackings agree well with the RPA findings. Besides, in the case of the TM selenides, DFT-D2 overestimates ΔE_0. The DFT-D2 binding energies are generally also overestimated but not as much as the vdW-DF E_b.

In Fig. 4(b) we compare the computed binding energy E_b. Apart from the DFT-D2 data for MoS_2, which are in excellent agreement with RPA, the errors are quite large in all other cases, but with important distinctions: First, DFT-D2 and vdW-DF have a general tendency for overbinding, whereas PBEsol predicts much less binding. Secondly, the good groups exhibit smaller deviations with respect to RPA than the bad ones, at least at DFT-D2 and vdW-DF level.

It was recently shown that the vdW E_b appears to be a universal quantity, which for a wide selection of bulk materials, characterized by different electronic and structural properties, fluctuates around 20 meV/Å^2 [82,83]. The only

TABLE III. Optimized interlayer distance d_0 (Å), the relative ground-state total energy ΔE_0 (meV/f.u., with respect to the most stable AA' stacking order), and binding energy E_b (meV/f.u.) as obtained by RPA, DFT-D2, vdW-DF (optB88), and PBEsol. For comparison available experimental data for d of the bulk $2H$ (stacking: AA') and $3R$ (stacking: AB) phases are also listed.

	RPA			DFT-D2			vdW-DF			PBEsol		
Stacking	d_0	ΔE_0	E_b	d_0	ΔE_0	E_b	d_0	ΔE_0	E_b	d_0	ΔE_0	E_b
MoS_2												
AA	6.77	33.3	47.9	6.87	29.2	44.8	6.77	35.1	73.4	7.37	12.8	2.4
AA'	6.27	0.0	81.2	6.24	0.0	74.1	6.23	0.0	108.5	6.32	0.0	15.0
$A'B$	6.78	34.3	45.4	6.84	27.8	46.3	6.77	33.4	75.1	7.37	12.6	2.7
AB	6.17	3.0	76.7	6.17	1.0	73.1	6.21	0.7	107.7	6.27	1.5	13.7
AB'	6.26	10.3	69.4	6.27	7.8	66.2	6.27	7.8	100.7	6.55	7.2	8.0
Expt. $2H$[a]	6.25											
Expt. $2H$[b]	6.15											
Expt. $3R$[c]	6.14											
$MoSe_2$												
AA	7.18	39.4	51.5	7.13	43.2	63.6	7.11	35.6	77.7	7.53	19.6	3.4
AA'	6.48	0.0	88.4	6.53	0.0	106.8	6.53	0.0	115.5	6.53	0.0	23.0
$A'B$	7.12	39.6	50.0	7.10	40.1	66.7	7.08	34.2	81.4	7.43	18.9	4.2
AB	6.47	4.5	85.1	6.53	1.8	105.4	6.51	1.6	113.9	6.55	2.1	20.8
AB'	6.53	13.5	76.2	6.63	11.2	95.7	6.61	11.1	104.4	6.79	10.7	12.3
Expt. $2H$[d]	6.45											
Expt. $3R$[e]	6.46											
WS_2												
AA	6.84	37.9	43.7	6.84	33.9	56.6	6.81	33.7	73.4	7.34	10.9	2.4
AA'	6.24	0.0	82.9	6.24	0.0	90.5	6.23	0.0	103.5	6.35	0.0	13.3
$A'B$	6.78	37.1	44.5	6.80	32.5	58.0	6.79	32.7	74.5	7.34	10.6	2.7
AB	6.24	7.3	74.3	6.24	1.7	88.9	6.22	1.5	105.7	6.38	1.9	11.4
AB'	6.27	14.6	67.0	6.24	9.6	81.0	6.31	9.2	98.0	6.64	6.9	6.5
Expt. $2H$[f]	6.16											
Expt. $3R$[f]	6.16											
WSe_2												
AA	7.24	38.0	48.7	7.09	49.3	76.5	7.13	37.7	77.30	7.54	18.1	3.4
AA'	6.50	0.0	89.9	6.54	0.0	125.9	6.54	0.0	115.0	6.60	0.0	21.5
$A'B$	7.24	39.6	48.3	7.08	46.7	79.0	7.09	37.7	77.3	7.44	17.4	4.1
AB	6.54	3.6	84.2	6.54	2.9	122.8	6.56	3.1	111.9	6.64	3.4	8.1
AB'	6.62	14.2	73.6	6.59	13.8	111.9	6.66	12.8	102.1	6.90	11.0	10.5
Expt. $2H$[g]	6.49											

[a]Reference [76].
[b]Reference [77].
[c]Reference [78].
[d]Reference [79].
[e]Reference [80].
[f]Reference [66].
[g]Reference [81].

significant exception is $PbTe_2$, with a binding energy of about 40 meV/Å^2 [82]. For the purpose of possibly generalizing this statement to the BL case we compare in Table IV our RPA E_b with the corresponding bulk data.

Besides including the pool of insulating BL AA' structured MX_2, we have performed additional RPA calculations for metallic TiS_2 and $PdTe_2$, as well as BL graphene. Our results correlate very well with the bulk values, extending the validity of the concept of universality to the low dimensional BL regime. We also confirm that $PdTe_2$ is an outliner also in the BL regime, with a binding energy of 50 meV/Å^2, 25% larger than the bulk value.

To investigate further the relative stability of the AA' and AB stackings we have computed the phonon free energy as a function of temperature [84] at vdW-DF level. The results shown in Fig. 5 suggest that for BL MoS_2 the AA' sequence would become the more stable phase as the temperature increases. This may explain that the predominantly observed BL MoS_2 in experiment exhibits the AA' stacking sequence.

To summarize this section, the following general remarks holding for all considered MX_2 are given:

(i) All methods correctly predict the AA' stacking to be the most favorable phase almost degenerate in energy with the AB stacking and deliver the same stability sequence characterized

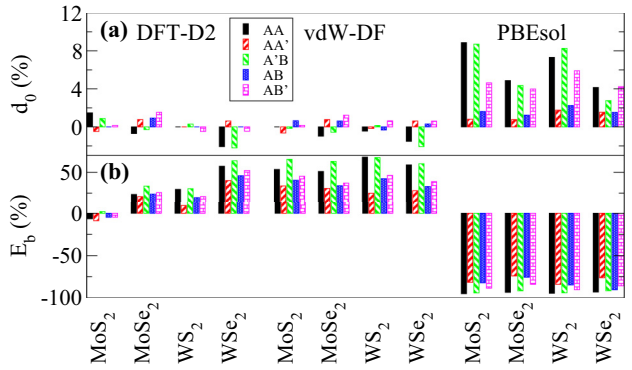

FIG. 4. (Color online) (a) Difference (in %) between the values of d_0 calculated by DFT-D2/vdW-DF/PBEsol, and the corresponding RPA results. (b) Relative deviation (in %) between the RPA and DFT-D2/vdW-DF/PBEsol values of the binding energy E_b.

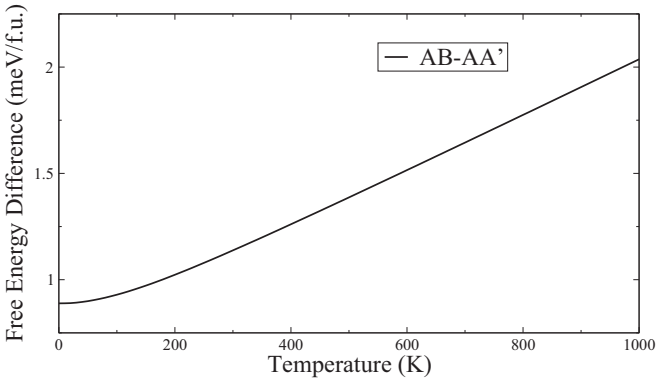

FIG. 5. Temperature-dependent free energy difference of the AA' and AB stackings at vdW-DF level.

by the distinction between good and bad stackings. However the relative stability of the various stackings with respect to the ground state AA' is quite different in RPA and DFT methods (see Table III). Free energy calculation shows that the AA' become progressively more stable for increasing temperature

(ii) The optimized interlayer distances d_0 of the good structures are almost identical to that of the corresponding bulk systems, whereas the bad structures have larger d_0 due to subtle balance between vdW and Pauli interactions.

(iii) The RPA description outperforms the standard DFT (PBEsol) and (to a lesser extent) vdW corrected DFT approaches (DFT-D2 and vdW-DF). Although the DFT methods with dispersion corrections yield very good d_0 and a correct stability sequence, the values of E_b are systematically overestimated. Owing to the lack of dispersion corrections PBEsol significantly overestimates the minimum interlayer distances (especially for the bad structures) and provides much to small E_b and ΔE_0.

Having established the most stable structures, the electronic and optical properties of the two most stable phases, AA' and AB, are discussed in the following section.

B. G_0W_0 electronic structure

It has been well established that ML MX_2 exhibits a direct gap with both, the conduction band minimum (CBM) and the valence band maximum (VBM) located at the K point [22]. As already mentioned in the introduction, *ab initio* and GW calculations have predicted that MX_2 undergo a direct-to-indirect gap crossover [21,32,34,40,45,85] in the BL as well as multilayer systems. In the case of MoS_2, angle-resolved photoemission spectroscopy (ARPES) measurements have recently confirmed this transition [86], which provides evidence on the shift of the VBM from K to Γ.

There are issues that remain still unexplored or controversial, such as the number and location of the valence band extrema and conduction band valleys [87]. More importantly, the role of the stacking order in the electronic and optical properties has not been addressed so far. In this section, we focus on the effects on the electronic properties of BL MX_2, which are examined within the G_0W_0+SOC approximation based on the equilibrium structures determined by using the RPA. For this purpose, the quasiparticle band structure of the MoS_2 for the five different stacking sequences are compared in Fig. 6. Qualitatively identical results are obtained for the other cases not shown here. The difference between good and bad stackings is reflected in the electronic dispersion: for all stackings the CBM is located at the T point, i.e., the midpoint between Γ and K (the notation in Ref. [88] is adopted). However, the VBM switches from Γ in the good structures to the K point in the bad structures, resulting in different types of indirect band gaps, which are indicated by arrows (green and red) in Fig. 6. The origin of this difference arises from the larger optimized interlayer distances in the bad structures as compared to the good ones, which are $d_0 = 6.77$ Å and 6.47 Å, for AA and AA' respectively (see Table III). This is further evidenced by the finding, that the energy difference between the highest occupied states at K and Γ is progressively reduced by decreasing the interlayer distance. Finally the valence band edge at Γ rises higher than the VBM at K for $d \approx d_0^{AA'}$.

In summary, the band structures of the good MoS_2 structures display very similar features, which are typical for all studied BL MX_2 compounds: (i) Contrary to ML MX_2, BL MX_2 are indirect semiconductors. (ii) Two distinct valence band edges are located at Γ and K. (iii) Three valleys in the conduction band are present at T, K, and Σ [88].

The complete set of G_0W_0+SOC results is summarized in Fig. 7, where the electronic band structures for BL MX_2 in the two most stable stackings, namely AA' and AB, are provided. First, no relevant differences between the AA' and AB stackings are observed apart from the additional band splitting in the AB order. This is due to the lack of inversion symmetry, which causes the formation of four bands (instead

TABLE IV. Comparison between the RPA binding energies E_b of BL and bulk materials. The bulk data are taken from Ref. [82]. The E_b for BL Graphene is compared to the graphite value given in Ref. [62]. The E_b is given in meV/Å^2 according to its definition in Ref. [82] for comparison.

	MoS_2	$MoSe_2$	WS_2	WSe_2	TiS_2	$PdTe_2$	Graphene
BL	18.78	18.88	19.26	19.28	19.47	50.27	17.37
Bulk	20.53	19.63	20.24	19.98	18.88	40.17	18.32

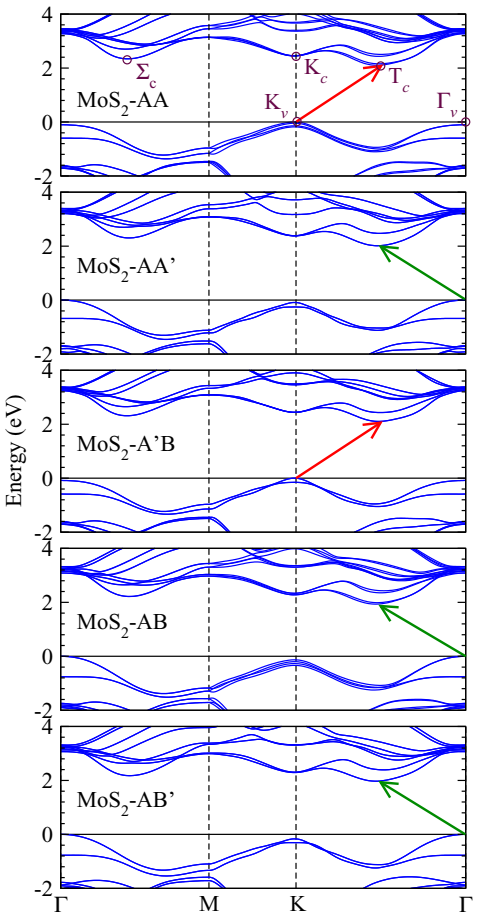

FIG. 6. (Color online) G_0W_0 quasiparticle band structures of AA, AA', $A'B$, AB, and AB' stacked bilayer MoS_2. Arrows indicate the direction of the indirect band gap. Spin-orbit coupling has been explicitly included in the G_0W_0 calculations. The valence band maxima and conduction band valleys are indicated with small circles and specific labels (subscript c/v stands for conduction/valence).

of two) along the M-K-Γ direction. Considering that the AA' and AB stackings are almost degenerate in energy this intimate relation between the stacking order and band splitting could serve as a fingerprint for the experimental identification of possible stacking faults. The recent ARPES data of Jin *et al.* pinpoint that exfoliated BL MoS_2 exhibits only two bands at K, a clear indication that BL MoS_2 adopts the AA' stacking order, in agreement with our RPA results.

Additional distinct features of the band structure include the location of the CBM that is found at point T for all structures, and the different relative position of the VBM which is situated at either Γ or K depending on the structure. In MoS_2 and WS_2 the VBM is at Γ, but in $MoSe_2$ and WSe_2 the VBM shifts to K, which is by 0.02 eV and 0.11 eV higher in energy in the latter two, respectively. This is again correlated with the vdW interlayer distance, which is significantly larger in the selenides ($d_0^{MoSe_2} = 6.48$ Å, $d_0^{WSe_2} = 6.50$ Å) than in sulfides ($d_0^{MoS_2} = 6.27$ Å, $d_0^{WS_2} = 6.24$ Å, see Table III). The change in the location of VBM when replacing the sulfur by the Se atoms in MX_2 could explain the qualitatively different temperature dependence of indirect transition in WSe_2 compared to MoS_2 and WS_2, which was recently observed by Zhao and coworkers, who addressed the energetics of the conduction band valleys by temperature-dependent photoluminescence measurements and standard PBE calculations [87].

The relative position of the conduction band valleys is an important issue for the interpretation and understanding of the optical and transport properties and is still controversial in the most extensively investigated mono- and few-layer MoS_2 [21,32,34,35,40,45,85,89].

One source of differences between the variety of published band structures of mono- and few-layer MX_2 is the theoretical approach employed in the calculations. Standard DFT calculations utilizing (semi)local exchange correlation functionals such as LDA or GGA are inadequate in describing the band structure of MX_2 [35,40], in particular the relative positions of the VBM at Γ and K, as well as the energy difference between the CBM at T and K. Quasiparticle calculations within the GW approximation (at least on the single-shot level G_0W_0) are indispensable for an accurate description of the band gaps and dispersions in these materials. Very recent G_0W_0+SOC calculations on ML and BL MoS_2 indicate that in the latter the lowest conduction band eigenvalue is at T, followed by a second valley roughly 100 meV higher at K, and the third valley at Σ [40], which is in agreement with our present findings. On the other hand, quasiparticle self-consistent GW (QSGW) calculations on BL MoS_2 [34] suggest the CBM to be located at K. As pointed out by the authors of this work as well as by Shi *et al.* [35], theoretical approaches that go even beyond the G_0W_0 approximation, such as partially self-consistent GW_0 (iterating the orbitals and eigenvalues in G only) or QSGW, need to be adopted to achieve a further refined description of the electronic properties of these materials.

A second source of inaccuracies arises from the structural details underlying the band structure calculations of monolayer and few-layer MX_2. In particular, the lattice constant, interlayer distance, and atomic positions defining the Mo-S bond length and S-Mo-S bond angle significantly affect the energy gaps and band dispersion. It was shown by Shi and coworkers [35] that ML MoS_2undergoes a transition to an indirect semiconductor, when increasing the lattice constant, i.e., under tensile strain of approximately 1.5%. The effect of confinement by changing the interlayer distance d on the band gap and optical transition energies in mono- and few-layer MoS_2 was investigated by Komsa *et al.* [32], who concluded that both, the indirect and direct gap in BL MoS_2 becomes larger with increasing d. Concerning the atomic positions, tests on ML MoS_2using standard LDA-DFT have revealed that the energy differences between K_c and T_c as well as K_v and Γ_v are significantly increased by relaxing the atomic positions. A subsequent G_0W_0 calculation based on these LDA-DFT wave functions again decreases both, the K_c-T_c and the K_v-Γ_v energy differences. Despite all these critical factors, all DFT+G_0W_0 studies agree in identifying ML MoS_2 as a direct band gap semiconductor. The omitted relaxations of the atomic positions could explain the residual energy difference of the valence band extrema at K and Γ in the present case compared to previous GW results on BL MoS_2 [34,40].

Finally, a third source for discrepancies in calculations is the proper treatment of spin-orbit coupling. As already emphasized, the inclusion of SOC is indispensable for a correct

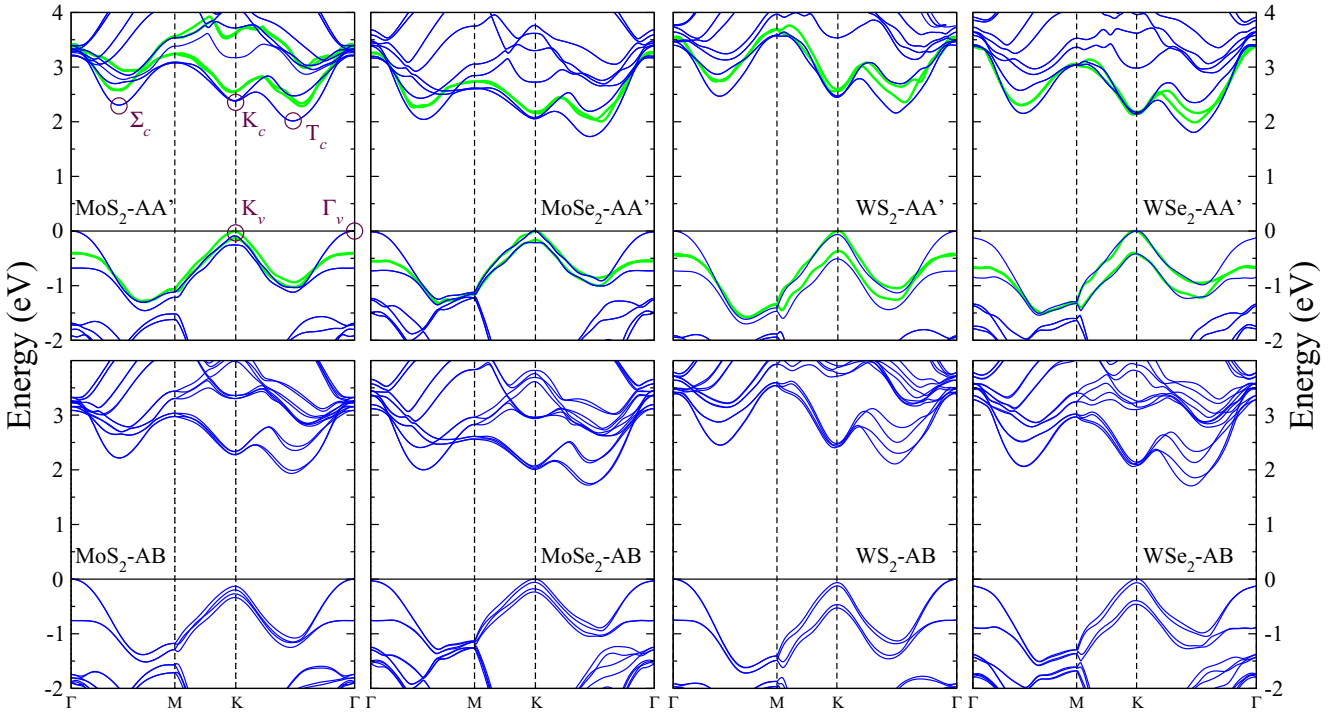

FIG. 7. (Color online) Quasiparticle band structures of AA' and AB stacked BL MX_2. The circles and the attached symbols indicate the positions of the conduction band valleys and valence band edges. Thick (green) lines show the monolayer band structure.

description of the absorption spectra of ML MX_2. For instance, in ML MoS_2 SOC is responsible for the small splitting ($\sim$0.2 eV) of the VBM at K, giving rise to the observation of the two A and B exciton peaks in photoluminescence experiments [22]. Notice that in multilayer and bulk MX_2, however, this splitting is due to the combination of intermolecular and spin-orbit interactions and the energy differences between the band extrema is not much changed by the SOC.

To complete this section and further analyze the band structures of MX_2, the interband transitions near the gap extracted from the G_0W_0+SOC band structures are collected in Table V. The listed energy differences have been evaluated from the valence and conduction band states (denoted by indices v and c, respectively) at the major band extrema Γ, K, T, and Σ as indicated in Fig. 7. For comparison, results of previous quasiparticle self-consistent GW (QSGW w/o SOC) [34] and G_0W_0+SOC [40] calculations on MoS_2 bilayer as well as available experimental data are included.

The direct K_c-K_v gap of AA'-MoS_2 is in good agreement with previous GW studies. Its overestimation by roughly 0.5 eV compared to experiment is explained by the missing electron-hole interactions (excitonic effects), which are strong in 2D materials due to confinement and lead to the formation of bound electron-hole pairs. These bound excitons reduce the direct band gap by their binding energy and define the optical gap, which is experimentally accessed by optical measurements such as photoluminescence or photoconductivity. Excitonic effects are addressed and discussed in the next section.

The indirect K_c-Γ_v transition in AA'-MoS_2 is larger by about 0.3–0.4 eV compared to previous GW results. This discrepancy originates from the subtle dependence of the band dispersions on the structural parameters as discussed above. In Ref. [34] the CBM is located at K yielding an indirect K_c-Γ_v gap of 1.89 eV, whereas in Ref. [40] the CBM is located at T defining an indirect T_c-Γ_v gap of 1.95 eV in perfect agreement with our finding of 1.96 eV. In all compounds, the AB interband transitions are generally marginally (less then 0.1 eV) smaller than the corresponding AA' values.

C. Optical absorption spectra

In this section, the effect of the stacking pattern on the optical properties is discussed. As already pointed out in the

TABLE V. Band gap and interband transitions in MX_2(in eV). Other GW(+SOC) and experimental data are listed, in brackets, when available.

Structures	K_c-K_v	K_c-Γ_v	T_c-K_v	T_c-Γ_v
MoS_2-AA'	2.41	2.32	2.05	1.96
	(2.43)[a]	(1.89)[a]		
	(2.32)[b]			(1.95)[b]
	(1.88)[c]	(1.6)[c]		
MoS_2-AB	2.29	2.12	1.98	1.82
$MoSe_2$-AA'	1.99	1.97	1.68	1.67
$MoSe_2$-AB	1.93	1.93	1.70	1.70
WS_2-AA'	2.48	2.38	2.15	2.05
WS_2-AB	2.40	2.33	2.05	1.98
WSe_2-AA'	2.08	2.18	1.71	1.81
WSe_2-AB	2.02	2.15	1.66	1.79

[a] $scGW$ calculations from Ref. [34].
[b] G_0W_0+SOC calculations from Ref. [40].
[c] Experimental values from Ref. [22].

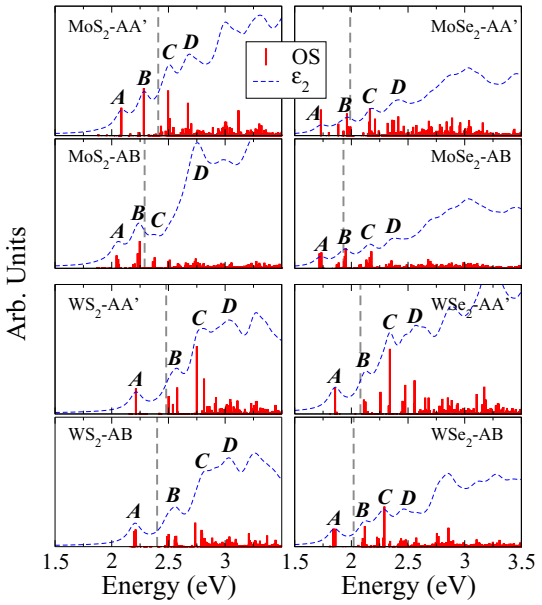

FIG. 8. (Color online) The optical absorption spectra. Frequency dependent imaginary part of the dielectric function ε_2 including excitonic effects (dashed lines) and the oscillator strengths (OS) of the optical transitions are given for the two most stable stacking sequences of MoS_2 and WS_2(left) as well as $MoSe_2$ and WSe_2 (right). The first four peaks are identified with the labels A, B, C, and D. Vertical dashed lines indicate the position of the K_c-K_v gap listed in Table V.

preceding section, due to the neglect of excitonic effects the G_0W_0 quasiparticle gap is usually larger than the measured optical gap. Now we take into account the electron-hole interactions by solving the Bethe-Salpeter equation using the quasiparticle wave functions and including SOC. The resulting optical absorption spectra are shown in Fig. 8 in terms of the frequency dependent imaginary part of the dielectric function ε_2 for the two most stable stacking patterns and the corresponding oscillator strengths.

As a general remark, the absorption spectra of BL MX_2 are found to be similar to the corresponding bulk ones. Below the smallest direct quasiparticle gap (see K_c-K_v column in Table V) excitonic peaks emerge in all structures. The splitting of the VBM at K induced by the interlayer interactions gives rise to the peak doublet (labeled A and B in Fig. 8), which is visible in both AA' and AB stacked structures. In the latter case, an additional tiny splitting is observed in the oscillator strengths of the optical transitions due to the lack of inversion symmetry in the AB stacking, which is in line with the splitting observed in the band structure at Γ and K (see the band structure in Fig. 7). Additional peaks appear at higher energies (labeled C and D in Fig. 8), which are again common to all considered systems. All these transitions are associated with excitations at K between d_{x^2}/d_{xy} (valence band) and d_{z^2} (conduction band) TM states.

For a more quantitative analysis, the energies of the optical transitions are listed together with the exciton binding energies of the lowest bound exciton in Table VI. We recall that the exciton binding energy is defined as the energy difference between the smallest direct quasiparticle gap and the optical transition energy.

TABLE VI. Excitonic optical transitions and the exciton binding energies $E_b^{e\text{-}h}$ of the lowest bound excitons A in MX_2 in units of (eV).

Structures	A	B	C	D	$E_b^{e\text{-}h}(A)$
MoS_2-AA'	2.08 (1.88)[a]	2.28 (2.05)[a]	2.50	2.67	0.33
MoS_2-AB	2.06	2.25	2.51	2.65	0.23
$MoSe_2$-AA'	1.73	1.96	2.16	2.41	0.26
$MoSe_2$-AB	1.73	1.96	2.18	2.35	0.20
WS_2-AA'	2.21	2.58	2.79	3.05	0.27
WS_2-AB	2.21	2.57	2.79	3.04	0.19
WSe_2-AA'	1.86	2.12	2.34	2.56	0.22
WSe_2-AB	1.86	2.12	2.29	2.48	0.16

[a]Experimental values from Ref. [22].

The optical transition energies are not significantly altered by the stacking pattern. The BL tungsten dichalcogenides exhibit a larger splitting of the VBM (see Fig. 7) resulting in a larger energy difference of the A and B excitons. Whereas this energy difference is ∼0.2 eV in the BL molybdenum dichalcogenides, it amounts to 0.37 eV and 0.26 eV in $WS_2$and WSe_2, respectively. The optical response of the disulfides (left column in Fig. 8) has higher energies (2.1–2.2 eV) than that of the diselenides (1.7–1.9 eV) in accordance with the quasiparticle band structure. For BL MoS_2, the only case for which a comparison with experiment is available, our data indicate that the BSE optical transitions are overestimated by about 0.2 eV, in line with previous BSE results [40].

The A exciton binding energies $E_b^{e\text{-}h}(A)$ in the AA' structures are 60 ∼ 100 meV larger than these in the AB stacked MX_2. Further, $E_b^{e\text{-}h}(A)$ is generally larger in sulfides (∼0.3 eV) than in the selenides (0.16–0.26 eV). The value of the B exciton binding energies $E_b^{e\text{-}h}(B)$ is always smaller than $E_b^{e\text{-}h}(A)$ and is determined by the by the energy splitting of the valence band maximum at K which gives raise to the double A-B peak structure. In the tungsten dichalcogenides, where the energy splitting at K is larger due to stronger SOC, the peak B lies slightly above the quasiparticle gap.

V. CONCLUSIONS

In this study, we have provided a comprehensive characterization of the structural, electronic and optical properties of bilayer transition metal dichalcogenides MX_2 (M = Mo and W; X = S and Se) in the many-body framework of RPA, G_0W_0, and BSE with the inclusion of spin-orbit coupling (SOC) effects. The combined accurate treatment of vdW interaction (RPA), electron correlation (G_0W_0), SOC, and excitonic effects (BSE) allowed the detailed description of this technologically relevant class of materials, which will serve as a guidance for the on-going experiments aiming to synthesize multilayer MX_2 and to optimize their optical properties for optoelectronic applications.

The RPA data indicate that the two bulklike AA' ($2H$) and AB ($3R$) stackings are almost degenerate in energy and exhibit qualitatively similar properties. The stability of these two phases is understood as a subtle competition between Pauli

and vdW interactions, and the vdW interlayer spacing is almost identical to the corresponding bulk value. The comparison with DFT-based approaches evidence that RPA outperform both PBEsol and, to a lesser extent, the vdW-corrected functionals DFT-D2 and vdW-DFT. More specifically, DFT-D2 and vdW-DF schemes yield very good interlayer distances, but suffer from large errors in the binding energies.

The band structure of the most stable structures show a similar shape, characterized by three distinct valleys at T, K, and Σ and a small energy splitting between the valence band maximum at K and Γ. The comparison with available experimental data for MoS_2 proves that the inclusion of SOC is essential to correctly describe and quantify the interband transition, especially the valence band maxima and conduction band minima. The different interlayer distance in sulfide ($d_0 \approx 6.2$ Å) and selenide ($d_0 \approx 6.5$ Å) BL systems originating from the different size of S and Se, is reflected in the value of the K_c-K_v gap, which is 0.4 eV larger in the transition metal sulfides. On the other hand, the M atom affects the degree of splitting (in particular at the conduction band minimum T, and at the valence band extrema at K and Γ) due to the different strength of the spin-orbit interaction in W and Mo.

Finally, the optical spectra elucidate the coupling between excitonic effects and SOC, with the appearance of a double-peak structure in all compounds. The exciton binding energy $E_b^{e\text{-}h}$ associated with the lowest exciton is the largest in the model system MoS_2 (≈0.3 eV) and is influenced by both, the chemical composition and the stacking. Concerning the former, the $E_b^{e\text{-}h}$ is larger for sulfides then selenides, and for a given chalcogenide it is larger for molybdenum than tungsten compounds. Regarding the stacking, the $E_b^{e\text{-}h}$ is smaller in the AB stacked structures.

To further exploit the physics of BL MX_2 via band engineering, it will be of great interest to study how the electronic and optical properties that we have accurately illustrated and discussed in this paper change with respect to external stimuli, such as strain [90], twisting [91,92], electric field [93], or doping [94].

ACKNOWLEDGMENTS

Research in Vienna was partially sponsored by the FP7 European Community grant ATHENA. Part of the calculations have been performed on the high-performance computing facility Vienna Scientific Cluster (VSC). We thank G. Kresse for useful discussions and for the critical reading of the manuscript. K.H. acknowledges the fruitful discussions with L. Wirtz and A. Molina-Sánchez.

[1] K. S. Novoselov, A. K. Geim, S. V. Morozov, D. Jiang, Y. Zhang, S. V. Dubonos, I. V. Grigorieva, and A. A. Firsov, Science **306**, 666 (2004).
[2] K. S. Novoselov, D. Jiang, F. Schedin, T. J. Booth, V. V. Khotkevich, S. V. Morozov, and A. K. Geim, P. Natl. Acad. Sci. USA **102**, 10451 (2005).
[3] K. S. Novoselov, A. K. Geim, S. V. Morozov, D. Jiang, M. I. Katsnelson, I. V. Grigorieva, S. V. Dubonos, and A. A. Firsov, Nature (London) **438**, 197 (2005).
[4] Y. Zhang, Y.-W. Tan, H. L. Stormer, and P. Kim, Nature (London) **438**, 201 (2005).
[5] A. K. Geim and K. S. Novoselov, Nature Mater. **6**, 183 (2007).
[6] A. K. Geim and K. S. Novoselov, Science **324**, 1530 (2009).
[7] J. N. Coleman *et al.*, Science **331**, 568 (2011).
[8] M. Z. Hasan and C. L. Kane, Rev. Mod. Phys. **82**, 3045 (2010).
[9] Q. H. Wang, K. Kalantar-Zadeh, A. Kis, J. N. Coleman, and M. S. Strano, Nature Nano **7**, 699 (2012).
[10] E. Doni and R. Girlanda, *Electronic Structure and Electronic Transitions in Layered Materials* (Springer-Verlag, Berlin, 1986).
[11] L. Liu, Y. P. Feng, and Z. X. Shen, Phys. Rev. B **68**, 104102 (2003).
[12] G. Constantinescu, A. Kuc, and T. Heine, Phys. Rev. Lett. **111**, 036104 (2013).
[13] D.-H. Cho, J.-S. Kim, S.-H. Kwon, C. Lee, and Y.-Z. Lee, Wear **302**, 981 (2013).
[14] I. Kaplan-Ashiri, S. R. Cohen, K. Gartsman, V. Ivanovskaya, T. Heine, G. Seifert, I. Wiesel, H. D. Wagner, and R. Tenne, Proc. Natl. Acad. Sci. USA **103**, 523 (2006).
[15] B. Lukose, A. Kuc, and T. Heine, Chem. Eur. J. **17**, 2388 (2011).
[16] Y. Kim, J.-L. Huang, and C. M. Lieber, Appl. Phys. Lett. **59**, 3404 (1991).
[17] E. Fortin and W. M. Sears, J. Phys. Chem. Solids **43**, 881 (1982).
[18] K. H. Hu, X. G. Hu, and X. J. Sun, Appl. Surf. Sci. **256**, 2517 (2010).
[19] *Gmelin Handbook of Inorganic and Organometallic Chemistry*, edited by L. Gmelin (Springer-Verlag, Berlin, 1995), Vol. B7, 8th ed.
[20] K. K. Kam and B. A. Parkinson, J. Phys. Chem. **86**, 463 (1982).
[21] A. Splendiani, L. Sun, Y. Zhang, T. Li, J. Kim, C.-Y. Chim, G. Galli, and F. Wang, Nano Lett. **10**, 1271 (2010).
[22] K. F. Mak, C. Lee, J. Hone, J. Shan, and T. F. Heinz, Phys. Rev. Lett. **105**, 136805 (2010).
[23] A. Klein, S. Tiefenbacher, V. Eyert, C. Pettenkofer, and W. Jaegermann, Phys. Rev. B **64**, 205416 (2001).
[24] K. Albe and A. Klein, Phys. Rev. B **66**, 073413 (2002).
[25] D. Voß, P. Krüger, A. Mazur, and J. Pollmann, Phys. Rev. B **60**, 14311 (1999).
[26] A. Rycerz, J. Tworzydlo, and C. W. J. Beenakker, Nature Phys. **3**, 172 (2007).
[27] K. F. Mak, K. He, J. Shan, and T. F. Heinz, Nature Nano **7**, 494 (2012).
[28] B. Radisavljevic, A. Radenovic, J. Brivio, V. Giacometti, and A. Kis, Nature Nano **6**, 147 (2011).
[29] L. Britnell, R. V. Gorbachev, R. Jalil, B. D. Belle, F. Schedin, A. Mishchenko, T. Georgiou, M. I. Katsnelson, L. Eaves, S. V. Morozov, N. M. R. Peres, J. Leist, A. K. Geim, K. S. Novoselov, and L. A. Ponomarenko, Science **335**, 947 (2012).
[30] C. Lee, H. Yan, L. E. Brus, T. F. Heinz, J. Hone, and S. Ryu, ACS Nano **4**, 2695 (2010).
[31] A. Molina-Sánchez and L. Wirtz, Phys. Rev. B **84**, 155413 (2011).
[32] H.-P. Komsa and A. V. Krasheninnikov, Phys. Rev. B **86**, 241201 (2012).
[33] A. Ramasubramaniam, Phys. Rev. B **86**, 115409 (2012).
[34] T. Cheiwchanchamnangij and W. R. L. Lambrecht, Phys. Rev. B **85**, 205302 (2012).

[35] H. Shi, H. Pan, Y.-W. Zhang, and B. I. Yakobson, Phys. Rev. B **87**, 155304 (2013).
[36] D. Y. Qiu, F. H. da Jornada, and S. G. Louie, Phys. Rev. Lett. **111**, 216805 (2013).
[37] L. Hedin, Phys. Rev. **139**, A796 (1965).
[38] F. Aryasetiawan and O. Gunnarsson, Rep. Prog. Phys. **61**, 237 (1998).
[39] W. Hanke and L. J. Sham, Phys. Rev. Lett. **43**, 387 (1979).
[40] A. Molina-Sánchez, D. Sangalli, K. Hummer, A. Marini, and L. Wirtz, Phys. Rev. B **88**, 045412 (2013).
[41] T. Li and G. Galli, J. Phys. Chem. C **111**, 16192 (2007).
[42] S. Lebègue and O. Eriksson, Phys. Rev. B **79**, 115409 (2009).
[43] S. W. Han, H. Kwon, S. K. Kim, S. Ryu, W. S. Yun, D. H. Kim, J. H. Hwang, J.-S. Kang, J. Baik, H. J. Shin, and S. C. Hong, Phys. Rev. B **84**, 045409 (2011).
[44] J. K. Ellis, M. J. Lucero, and G. E. Scuseria, Appl. Phys. Lett. **99**, 261908 (2011).
[45] W. S. Yun, S. W. Han, S. C. Hong, I. G. Kim, and J. D. Lee, Phys. Rev. B **85**, 033305 (2012).
[46] D. M. Ceperley and B. J. Alder, Phys. Rev. Lett. **45**, 566 (1980).
[47] J. P. Perdew, K. Burke, and M. Ernzerhof, Phys. Rev. Lett. **77**, 3865 (1996).
[48] S. Grimme, J. Comput. Chem. **27**, 1787 (2006). We made use of the following DFT-D2 parameter: Mo: $C_6 = 24.67$, $R_0 = 1.639$; W: $C_6 = 42.44$, $R_0 = 1.750$; S: $C_6 = 5.57$, $R_0 = 1.683$; Se: $C_6 = 12.64$, $R_0 = 1.771$.
[49] A. Tkatchenko and M. Scheffler, Phys. Rev. Lett. **102**, 073005 (2009).
[50] J. Klimeš and A. Michaelides, J. Chem. Phys. **137**, 120901 (2012).
[51] T. Bučko, J. Hafner, S. Lebègue, and J. G. Ángyán, J. Phys. Chem. A **114**, 11814 (2010).
[52] T. Bučko, S. Lebègue, J. Hafner, and J. G. Ángyán, Phys. Rev. B **87**, 064110 (2013).
[53] M. Dion, H. Rydberg, E. Schröder, D. C. Langreth, and B. I. Lundqvist, Phys. Rev. Lett. **92**, 246401 (2004).
[54] J. Klimeš, D. R. Bowler, and A. Michaelides, Phys. Rev. B **83**, 195131 (2011).
[55] J. F. Dobson and B. P. Dinte, Phys. Rev. Lett. **76**, 1780 (1996).
[56] H. Ehrenreich and M. H. Cohen, Phys. Rev. **115**, 786 (1959).
[57] M. Fuchs and X. Gonze, Phys. Rev. B **65**, 235109 (2002).
[58] J. Harl, L. Schimka, and G. Kresse, Phys. Rev. B **81**, 115126 (2010).
[59] C. Pisani, L. Maschio, S. Casassa, M. Halo, M. Schtz, and D. Usvyat, J. Comput. Chem. **29**, 2113 (2008).
[60] A. Marini, P. García-González, and A. Rubio, Phys. Rev. Lett. **96**, 136404 (2006).
[61] F. Mittendorfer, A. Garhofer, J. Redinger, J. Klimeš, J. Harl, and G. Kresse, Phys. Rev. B **84**, 201401(R) (2011).
[62] S. Lebègue, J. Harl, T. Gould, J. G. Ángyán, G. Kresse, and J. F. Dobson, Phys. Rev. Lett. **105**, 196401 (2010).
[63] T. Olsen, J. Yan, J. J. Mortensen, and K. S. Thygesen, Phys. Rev. Lett. **107**, 156401 (2011).
[64] K. D. Bronsema, J. L. De Boer, and F. Jellinek, Z. Anorg. Allg. Chem. **540**, 15 (1986).
[65] R. Coehoorn, C. Haas, J. Dijkstra, C. J. F. Flipse, R. A. de Groot, and A. Wold, Phys. Rev. B **35**, 6195 (1987).
[66] W. Schutte, J. D. Boer, and F. Jellinek, J. Solid State Chem. **70**, 207 (1987).
[67] G. Kresse and J. Hafner, Phys. Rev. B **48**, 13115 (1993).
[68] G. Kresse and J. Furthmüller, Comput. Mater. Sci. **6**, 15 (1996).
[69] P. E. Blöchl, Phys. Rev. B **50**, 17953 (1994).
[70] G. Kresse and D. Joubert, Phys. Rev. B **59**, 1758 (1999).
[71] J. P. Perdew, A. Ruzsinszky, G. I. Csonka, O. A. Vydrov, G. E. Scuseria, L. A. Constantin, X. Zhou, and K. Burke, Phys. Rev. Lett. **100**, 136406 (2008).
[72] D. Tunega, T. Bučko, and A. Zaoui, J. Chem. Phys. **137**, 114105 (2012).
[73] A. A. Mostofi, J. R. Yates, Y.-S. Lee, I. Souza, D. Vanderbilt, and N. Marzari, Comput. Phys. Commun. **178**, 685 (2008).
[74] C. Franchini, R. Kováčik, M. Marsman, S. S. Murthy, J. He, C. Ederer, and G. Kresse, J. Phys.: Condens. Matter **24**, 235602 (2012).
[75] N. Marom, J. Bernstein, J. Garel, A. Tkatchenko, E. Joselevich, L. Kronik, and O. Hod, Phys. Rev. Lett. **105**, 046801 (2010).
[76] N. Wakabayashi, H. G. Smith, and R. M. Nicklow, Phys. Rev. B **12**, 659 (1975).
[77] S. Srivastava, B. Avasthi, and B. Mathur, J. Mater. Sci. Lett. **3**, 671 (1984).
[78] Y. Takeuchi and W. Nowacki, Schweiz. Miner. Petrog. **44**, 105 (1964).
[79] P. B. James and M. T. Lavik, Acta Crystallogr. **16**, 1183 (1963).
[80] L. C. Towle, V. Oberbeck, B. E. Brown, and R. E. Stajdohar, Science **154**, 895 (1966).
[81] V. L. Kalikhman, Izv. Akad. Nauk SSSR. Neorg. Mater. **19**, 1060 (1983).
[82] T. Björkman, A. Gulans, A. V. Krasheninnikov, and R. M. Nieminen, Phys. Rev. Lett. **108**, 235502 (2012).
[83] T. Björkman, A. Gulans, A. V. Krasheninnikov, and R. M. Nieminen, J. Phys.: Condens. Matter **24**, 424218 (2012).
[84] A. Togo, F. Oba, and I. Tanaka, Phys. Rev. B **78**, 134106 (2008).
[85] A. Ramasubramaniam, D. Naveh, and E. Towe, Phys. Rev. B **84**, 205325 (2011).
[86] W. Jin, P.-C. Yeh, N. Zaki, D. Zhang, J. T. Sadowski, A. Al-Mahboob, A. M. van der Zande, D. A. Chenet, J. I. Dadap, I. P. Herman, P. Sutter, J. Hone, and R. M. Osgood, Jr., Phys. Rev. Lett. **111**, 106801 (2013).
[87] W. Zhao, R. M. Ribeiro, M. Toh, A. Carvalho, C. Kloc, A. H. Castro Neto, and G. Eda, Nano Lett. **13**, 5627 (2013).
[88] A. P. Cracknell, Thin Solid Films **21**, 107 (1974). Same notations are used in: G.F. Roster *Space Groups and Their Representations* (Academic Press, New York, 1957).
[89] A. Kuc, N. Zibouche, and T. Heine, Phys. Rev. B **83**, 245213 (2011).
[90] Andres Castellanos-Gomez, Rafael Roldn, Emmanuele Cappelluti, Michele Buscema, Francisco Guinea, Herre S. J van der Zant, and Gary A. Steele, Nano Lett. **13**5361 (2013).
[91] Jun Kang, Jingbo Li, Shu-Shen Li, Jian-Bai Xia and Lin-Wang Wang, Nano Letters **13**, 5485 (2013).
[92] Arend M. van der Zande, Pinshane Y. Huang, Daniel A. Chenet, Timothy C. Berkelbach, YuMeng You, Gwan-Hyoung Lee, Tony F. Heinz, David R. Reichman, David A. Muller, and James C. Hone, Nature Mater. **12**, 554 (2013).
[93] Andres Castellanos-Gomez, Emmanuele Cappelluti, Rafael Roldán, Nicolás Agraït, Francisco Guinea, and Gabino Rubio-Bollinger, Adv. Mater. **25**, 899 (2013).
[94] Shinichiro Mouri, Yuhei Miyauchi, and Kazunari Matsuda, Nano Lett. **13**, 5944 (2013).